

Stable blue phosphorescent organic LEDs that use polariton-enhanced Purcell effects

<https://doi.org/10.1038/s41586-023-06976-8>

Haonan Zhao¹, Claire E. Arneson¹, Dejiu Fan² & Stephen R. Forrest^{1,2,3}✉

Received: 15 April 2023

Accepted: 14 December 2023

Published online: 20 December 2023

 Check for updates

Phosphorescent organic light-emitting diodes (PHOLEDs) feature high efficiency^{1,2}, brightness and colour tunability suitable for both display and lighting applications³. However, overcoming the short operational lifetime of blue PHOLEDs remains one of the most challenging high-value problems in the field of organic electronics. Their short lifetimes originate from the annihilation of high-energy, long-lived blue triplets that leads to molecular dissociation^{4–7}. The Purcell effect, the enhancement of the radiative decay rate in a microcavity, can reduce the triplet density and, hence, the probability of destructive high-energy triplet–polaron annihilation (TPA)^{5,6} and triplet–triplet annihilation (TTA) events^{4,5,7,8}. Here we introduce the polariton-enhanced Purcell effect in blue PHOLEDs. We find that plasmon–exciton polaritons⁹ (PEPs) substantially increase the strength of the Purcell effect and achieve an average Purcell factor (PF) of 2.4 ± 0.2 over a 50-nm-thick emission layer (EML) in a blue PHOLED. A 5.3-fold improvement in LT90 (the time for the PHOLED luminance to decay to 90% of its initial value) of a cyan-emitting Ir-complex device is achieved compared with its use in a conventional PHOLED. Shifting the chromaticity coordinates to (0.14, 0.14) and (0.15, 0.20) into the deep blue, the Purcell-enhanced devices achieve 10–14 times improvement over similarly deep-blue PHOLEDs, with one structure reaching the longest Ir-complex device lifetime of $LT90 = 140 \pm 20$ h reported so far^{10–21}. The polariton-enhanced Purcell effect and microcavity engineering provide new possibilities for extending deep-blue PHOLED lifetimes.

PHOLEDs have been extensively used in both display and lighting applications owing to their vibrant colours and high efficiencies. However, because degradation is fundamentally energy-driven^{4–7}, blue PHOLEDs used in displays have unacceptably short lifetimes^{10–22} compared with green and red PHOLEDs³. The primary, energetically driven mechanisms leading to short blue PHOLED lifetimes are TPA (refs. 5,6) and/or TTA (refs. 4,5,7). These reactions approximately double the energy of the excited states up to approximately 6.0 eV (refs. 4,11), which is sufficient to break intramolecular bonds and convert an organic molecule to a nonradiative quenching centre^{5,7,10,11}.

To minimize the probability for high-energy annihilation events while maintaining high efficiency, the triplet density should be reduced using rapid radiative energy transfer. An OLED is, by nature, a weak multimode microcavity²³ comprising outcoupled and waveguided modes in the organic and substrate layers and surface plasmon polaritons (SPPs), among others⁴. The enhancement of the radiative decay rates using a microcavity, known as the Purcell effect, can reduce the triplet density to approximately the inverse of the PF (refs. 5,8) and thereby reduce the probability for TPA and/or TTA (see Methods). Here the PF is the triplet radiative decay rate in the OLED microcavity normalized by its natural radiative decay rate, that is, $PF = k_t/k_{r,0}$. However, as depicted in Fig. 1a, in a conventional PHOLED, the weak triplet energy transfer to conventional metal-cathode SPPs induces only a modest change in the decay rate, leaving a high triplet density at equilibrium. A promising

approach to enhance decay rates was reported by Fusella et al.²⁴, who doubled the lifetime of a green PHOLED by means of energy transfer from triplets to SPPs in a thin top metal cathode containing a random array of Ag nanocubes for top-emission extraction. However, this technique introduces complexity that is incompatible with full-colour, stable and scalable displays manufacturing.

In this work, we introduce the polariton-enhanced Purcell effect to extend the operational lifetime of blue PHOLEDs. We demonstrate that energy transfer to PEPs substantially reduces the triplet radiative lifetime and their density within the PHOLED EML. PEPs are a strongly coupled state at the metal–dielectric interface^{9,25} resulting from mixing of the SPP mode with excitons in the adjacent dielectric. Here the PEP strength is a function of the oscillator strengths of both the cathode and the electron transport layer (ETL) (see Fig. 1b). Combined with a low-quality-factor (Q) optical cavity comprising a Ag cathode + a distributed Bragg reflector (DBR) mirror, the light extraction efficiency and the emission colour saturation are increased.

Three archetype devices are made to maximize the total deep-blue-photon output featuring long device lifetime, saturated emission and high external quantum efficiency (EQE). By engineering the PEP-enhanced Purcell effect, we demonstrate a deep-blue $\text{Ir}(\text{dmp})_3$ -based PHOLED with an average PF of 2.4 ± 0.2 across the 50-nm-thick EML, leading to a 5.3-fold increase in LT90 compared with a conventional PHOLED using this same phosphor. By optimizing the Ag/DBR

¹Department of Physics, University of Michigan, Ann Arbor, MI, USA. ²Department of Electrical Engineering and Computer Science, University of Michigan, Ann Arbor, MI, USA. ³Department of Materials Science and Engineering, University of Michigan, Ann Arbor, MI, USA. ✉e-mail: stevefor@umich.edu

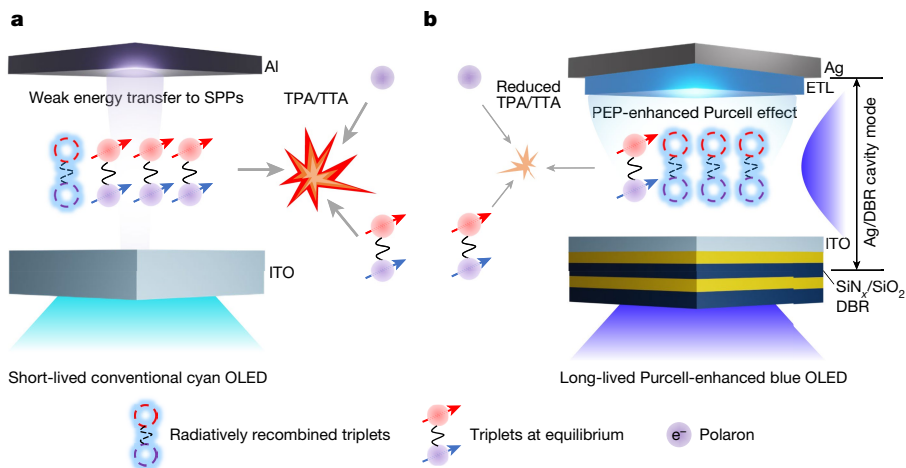


Fig. 1 | The PEP-enhanced Purcell effect. **a**, Cyan-emitting conventional devices. Triplets have a small energy transfer rate to the SPPs at the cathode surface and thus only a moderate change in the PL lifetime. The slow radiative decay of triplets results in a large density at equilibrium, inducing a high probability for TPA and TTA, leading to rapid degradation. **b**, Deep-blue-emitting

cavity devices using a Ag/ETL combination, leading to an enhanced Purcell effect by means of fast energy transfer to PEPs. Consequently, the triplet density is reduced, thereby reducing TPA and TTA. The Purcell-enhanced devices use DBRs to form an optical cavity with the metal cathode to improve light extraction and emission colour saturation.

cavity, the Commission Internationale d'Eclairage (CIE) coordinates of the conventional $\text{Ir}(\text{dmp})_3$ PHOLED shifted from cyan at (0.16, 0.26) to deep blue at (0.14, 0.14), gaining an almost threefold increase in LT90 using the Purcell effect enhanced by the strong Ag SPP, while maintaining the same EQE. Considering the prolonged device operational lifetime and saturated colour, the device achieves a 14 times enhancement in LT90 compared with other, similarly deep-blue Ir -complex-based PHOLEDs. By balancing the EQE and the PF, a PEP-enhanced device using Ag cathode/BPyTP2 ETL achieves the longest normalized LT90 of 140 ± 20 h at CIE = (0.15, 0.20) among Ir -complex-based PHOLEDs with $\text{CIE}_y < 0.31$ reported so far^{10–21}.

PEP and SPP dispersion engineering

A strongly coupled PEP state⁹ is formed at the metal cathode–ETL interface at wavelengths at which the ETL singlet exciton is resonant with the SPP mode of the cathode (see Extended Data Fig. 1 for chemical structures of the molecules used). Figure 2a,b shows the match between the measured and calculated angle-resolved spectra, respectively. The strongly coupled PEPs for the Al/BPyTP2 combination dispersion splits into upper polariton (UP), middle polariton (MP) and lower polariton (LP) branches. Owing to the large oscillator strength of BPyTP2 at energies slightly above the blue phosphor $\text{Ir}(\text{dmp})_3$ triplet of 2.8–3.0 eV (refs. 4,11,16), an anticrossing is formed between the Al SPP and excitons in the ETL, resulting in a relatively flat, redshifted LP dispersion at $\lambda = 400\text{--}500$ nm (see Extended Data Fig. 2 and Methods for the analysis of the PEPs). When BPyTP2 is replaced by another common ETL, SF3Trz, the polariton redshift is weaker owing to the higher SF3Trz exciton energy²⁶. The overlap between the Al/BPyTP2 LP energy and the $\text{Ir}(\text{dmp})_3$ triplet emission is, therefore, larger than the Al/SF3Trz polariton. Using a Ag cathode, the splitting between the BPyTP2 exciton and the Ag/BPyTP2 PEP dispersion is even larger owing to the stronger SPP in Ag than in Al. The MP and UP branches are not observed owing to their higher energy than the Ag absorption band. The Ag/BPyTP2 PEP has an asymptotically flat region limited by the BPyTP2 exciton energy at $1 < k_x/k_0 < \infty$. Here k_0 is the wavevector in vacuum. Therefore, Ag/BPyTP2 shows the most complete overlap between the PEP and the blue–cyan region at wavelengths of 400–500 nm, followed by Ag/SF3Trz > Al/BPyTP2 > Al/SF3Trz.

Figure 2c shows the angular photoluminescence (PL) of the same structures as in Fig. 2a,b. The Ag/BPyTP2 PEP LP branch shows a PL

intensity that is two orders of magnitude higher than the other three cathode/ETLs, indicating enhanced mixing between the SPP and ETL excitons. Note that the strong coupling is between the ETL and the cathode, and the triplet from the blue phosphor emission is transferred to the PEPs in the weak-coupling regime owing to the low oscillator strength of triplets.

Purcell effect and energy transfer rates

Figure 3a shows several PHOLED structures labelled as C, H and F (see Extended Data Fig. 3 for details of all the devices studied). Compared with device C that has a conventional Al cathode and an indium tin oxide (ITO) anode, the half-cavity device H uses a Ag cathode buffered by a 3-nm-thick Al layer supporting enhanced energy transfer to polariton modes. The full-cavity device F is identical to H except that it features a bottom DBR + the top Ag cathode low- Q cavity used to tune the emission colour. The calculated distribution of radiative and nonradiative channels at 465–475 nm in the three archetype $\text{Ir}(\text{dmp})_3$ devices is illustrated in the histograms of Fig. 3a, whereas the optical density of states (ODoS) distributions are shown in Extended Data Fig. 4a. Compared with the weak energy transfer to the Al SPP in C, the ODoS and the PF are increased through enhanced polariton energy transfer near the Ag/BPyTP2 or Ag/SF3Trz in devices H and F.

The generation of defects by TPA/TTA is reduced via decreasing the triplet density by increasing the radiative rate, which is directly proportional to the PF. The defect generation rate is consequently slowed in devices H and F, indicated by the shorter red arrows in Fig. 3a. On the other hand, given the same loss in PL quantum yield, η_{PL} , a larger defect density is required in devices H and F to match the increased radiative energy transfer at LT85, indicated by the larger dashed rectangular area. This suggests a nonlinear dependence between device lifetime and the PF (see Methods). The Ag/DBR cavity mode in F increases the outcoupling efficiency compared with H, corresponding to $k_x/k_0 < 1$, by placing the EML at the antinode of the Ag/DBR cavity mode⁴. Consequently, the Ag/DBR cavity device F features a large PF, an enhanced EQE compared with H and a narrowed emission spectrum.

Figure 3b shows time-resolved PL (TrPL) of a 50-nm-thick $\text{Ir}(\text{cb})_3$ EML in structures C, H and F. Here we study $\text{Ir}(\text{cb})_3$ because of its high $\eta_{\text{PL}} = 85 \pm 8\%$ (ref. 16) relative to $\text{Ir}(\text{dmp})_3$, as well as to understand the generality of the effects. Samples H and F with a Ag cathode have larger k_r than those with an Al cathode (C); those with a BPyTP2 ETL have a

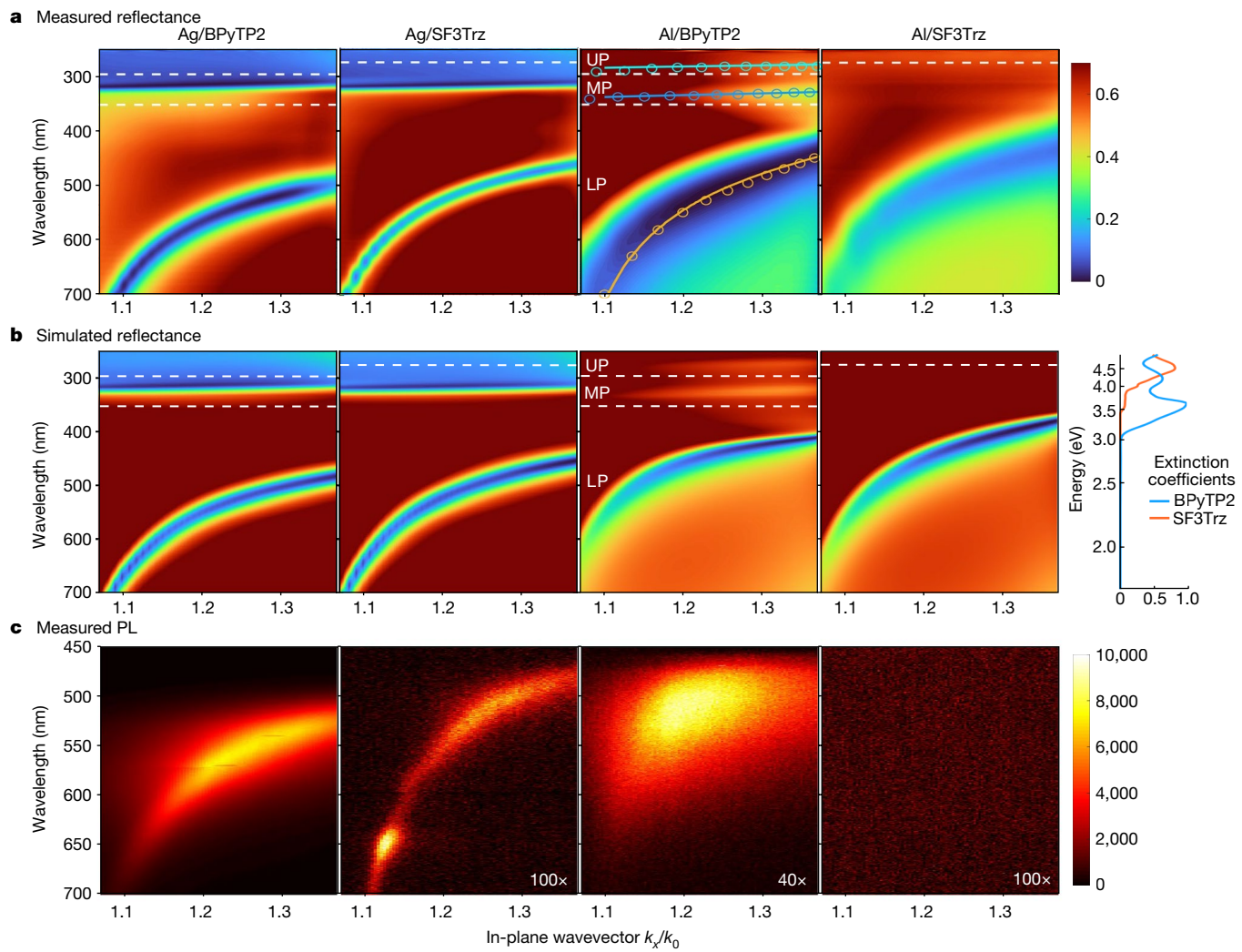


Fig. 2 | Polariton dispersion engineering. Angle-resolved polariton dispersion of (from left to right) Ag/BPyTP2, Ag/SF3Trz, Al/BPyTP2 and Al/SF3Trz cathode/ETLs. **a**, Measured reflectance using ellipsometry. The Al/BPyTP2 LP, MP and UP are fitted to the corrected local minima (circles) using the coupled oscillator model, labelled by solid lines. **b**, Simulated reflectance using transfer-matrix methods. The extinction coefficients of BPyTP2 and SF3Trz are shown in the

right-hand panel. BPyTP2/SF3Trz exciton absorption peak fits are labelled by dashed lines. The colour bar is for both measurement (**a**) and simulation (**b**). **c**, Angular PL measured using Fourier imaging spectroscopy. The PL intensities are multiplied by 100×, 40× and 100× for Ag/SF3Trz, Al/BPyTP2 and Al/SF3Trz, respectively. See Methods and Extended Data Fig. 2 for analysis of the PEP dispersion.

larger radiative rate, k_r , than those with SF3Trz, following the trend of the polariton dispersion in Fig. 2. Full Ag/DBR cavity samples show a negligible change compared with half cavities, indicating that the low- Q Ag/DBR cavity mode has little impact on the PF. By increasing energy transfer to SPPs or PEPs in the transverse magnetic (TM) modes, the PL becomes dominated by the horizontally aligned triplets (see Extended Data Fig. 4b,c). We estimate the average PF for isotropic orientation by comparing measurement and simulation (see Extended Data Fig. 4b-d and Methods for detailed analysis). Cavity F using a 15-nm-thick BPyTP2 ETL results in an average PF of 2.4 ± 0.2 , followed by PFs of 1.9 ± 0.2 and 1.40 ± 0.03 for F and C devices, respectively (see Extended Data Fig. 4 and Methods).

PHOLED performance

Figure 4a,b shows the EQE and electroluminescent (EL) spectrum of devices C1–C3 and F1–C3 using a cyan-emitting mCBP:Ir(dmp)₃ graded EML with $\eta_{PL} = 44 \pm 1\%$ (refs. 10,11) (see Table 1 and Extended Data Table 1 for device performance data). Structure 1 uses a 17-nm-thick SF3Trz ETL featuring only SPP energy transfer, whereas 2 and 3 use 17-nm-thick and

25-nm-thick BPyTP2 ETL, respectively, for PEP energy transfer. F1 has a PF of 1.9 ± 0.2 and shifts the CIE coordinates of C1 from (0.16, 0.26) to (0.14, 0.14) while maintaining the same EQE. With a similar ETL thickness, device F2 has a PF of 2.4 ± 0.2 and shifts the CIE coordinates to (0.14, 0.18), whereas it suffers from EQE loss owing to the strong energy transfer to PEPs. The ETL thickness of F3 is optimized to balance the trade-off between PF and EQE, resulting in a PF of 2.0 ± 0.2 , a deep-blue colour of CIE = (0.15, 0.20) and a peak EQE of $10.4 \pm 0.5\%$, compared with the corresponding device C3 with EQE of $9.9 \pm 0.1\%$ and CIE = (0.16, 0.27). Given that surface polariton modes exponentially decay in the out-of-plane direction, the PEP-enhanced F3 with a thicker ETL still features a slightly higher PF than the SPP-enhanced F1, along with a 45% increase in outcoupling efficiency. Besides converting the cyan emission into the deep blue, the low- Q Ag/DBR cavity mode has only a small impact on the angular dependence of the emission spectrum, shown by F2 in Fig. 4c. The angular dependence of the emission intensity of F2 differs only slightly from C2 (see inset). From C to F, the current–voltage characteristics show no change in devices using the same ETL (see Extended Data Fig. 5d, indicating that there is no power penalty associated with this device design).

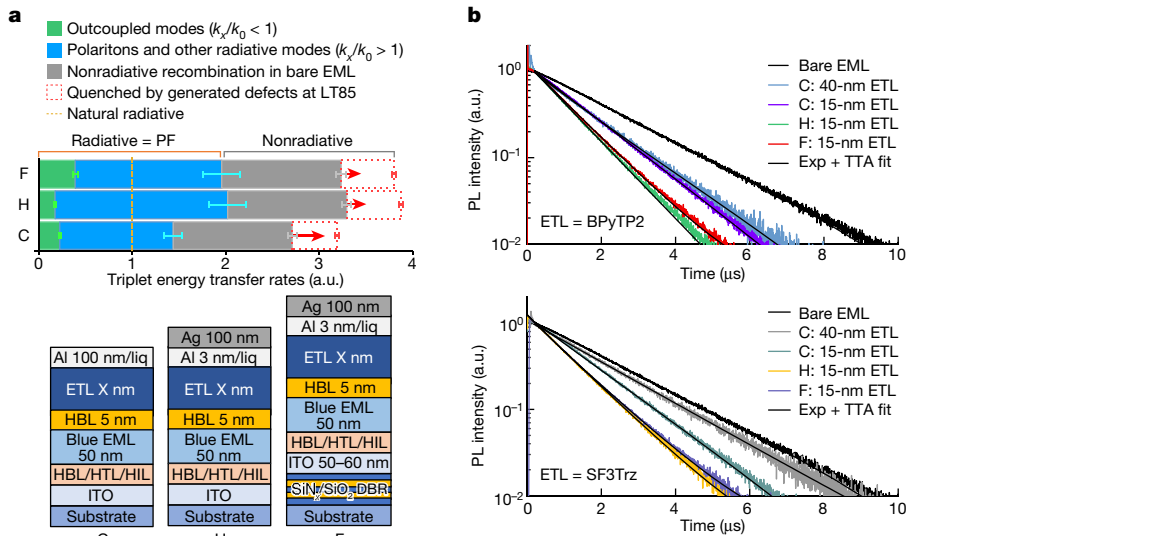


Fig. 3 | Optical engineering of blue PHOLEDs. **a**, Structures of conventional PHOLEDs, C, with an Al/Liq cathode; a polariton-enhanced half cavity, H, with Ag cathode buffered by 3-nm-thick Al and Liq; a full cavity, F, by adding a bottom DBR to H. All structures include a 50-nm-thick EML. Top, triplet energy transfer rates for different channels are shown for Ir(dmp)₃ devices C3, H3 and F3, normalized to the natural radiative decay rate (dashed orange line). Radiative channels include outcoupled modes with $k_x/k_0 < 1$ and high- k_x modes, and ODoS for C, H and F at 465–475 nm are shown. Nonradiative channels include

nonradiative recombination in the EML (grey) and quenching by defects (red). Error bars indicate the standard deviation of measured or calculated energy transfer rates. Red arrows indicate the growing fraction of nonradiative quenching by defects generated during ageing. Dashed rectangles indicate the generated defect density at LT85. **b**, TrPL spectra for 50-nm-thick Ir(cb)₃ EML structures C, H and F (see Methods and Extended Data Fig. 4 for details). All data are fitted to the TTA model as well as to a single exponential decay. a.u., arbitrary units.

Figure 4d shows the operational lifetime of F1–F3 compared with C1–C3. Aged at a current density of $J = 7 \text{ mA cm}^{-2}$ (corresponding to an initial luminance of $L_0 \approx 1,000 \text{ cd m}^{-2}$ for cyan-emitting C3; see Table 1) a 4.4 times enhancement in LT90 is achieved from the most strongly

Purcell-enhanced F2 from C2, compared with 2.5 times for F1 versus C1 and 2.2 times from F3 to C3. Figure 5a summarizes the Ir(dmp)₃ device operational lifetime versus the calculated average PF. From LT90 to LT70, the power law between the operational lifetime versus

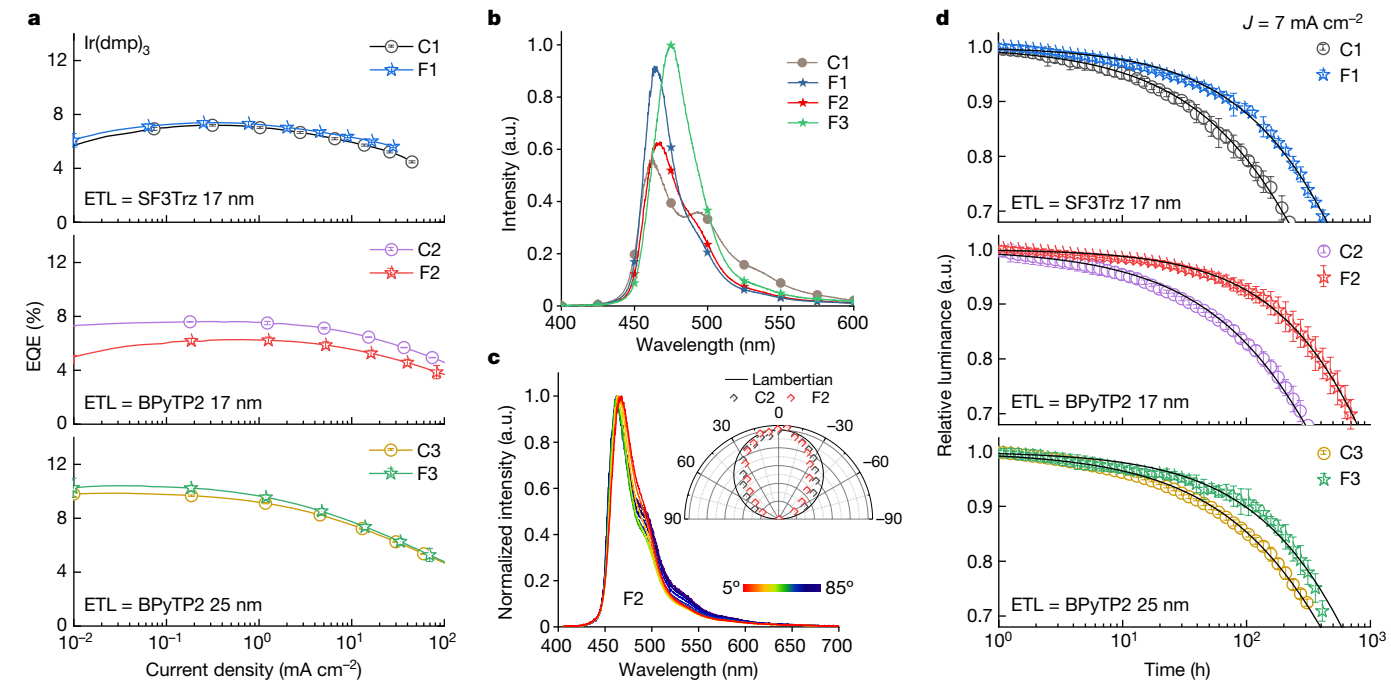


Fig. 4 | Ir(dmp)₃ device performance. **a**, EQE versus current density (J) for Ir(dmp)₃ devices C1–C3 and F1–F3. **b**, EL intensity spectra for C1 and F1–F3. The relative EL intensity calculated on the basis of the EQE at $J = 10 \text{ mA cm}^{-2}$ is shown. **c**, Angle-resolved PL spectra for F2. Inset, angle-resolved PL intensity of F2 and C2. The Lambertian emission is labelled by the solid black line. **d**, Luminance decay for C1–C3 and F1–F3 at $J = 7 \text{ mA cm}^{-2}$ (corresponding to an approximate initial luminance of about $1,000 \text{ cd m}^{-2}$ for C3; see Table 1). The first structure uses a 17-nm-thick SF3Trz ETL and the second and third structures use

17-nm-thick and 25-nm-thick BPYTP2 ETLs, respectively. Solid black lines are fits to a stretched exponential: $L(t)/L_0 = \exp[-(t/t_0)^\beta]$, in which L_0 is the initial luminance and t_0 and β are parameters (see Extended Data Table 2). Error bars indicate the 95% confidence interval of the luminance data within every 0.03 decade. For C1–C3, H1–H3 and F1, lifetime data are averaged from two devices in different batches. For F2 and F3, lifetime data are averaged from three devices in different batches. See detailed data plots in Extended Data Fig. 5. a.u., arbitrary units.

Article

Table 1 | Summary of Ir(dmp)₃ PHOLED performance, in which device performances for control (C) and full (F) cavity devices are compared

No.	Cavity structure ^a	EQE _{max} (%) ^b	Calculated PF _{avg} ^c	CIE	L ₀ (cd m ⁻²) ^d	LT90 (h) ^d	LT70 (h) ^d
7 mA cm⁻²							
C1	Al/SF3Trz 17 nm//ITO	7.2 ± 0.1	1.4 ± 0.1	(0.16, 0.26)	770 ± 10	30 ± 5	200 ± 30
F1	Ag/SF3Trz 17 nm//DBR	7.4 ± 0.2	1.9 ± 0.2	(0.14, 0.14)	500 ± 20	75 ± 10	400 ± 20
C2	Al/BPyTP2 17 nm//ITO	7.6 ± 0.1	1.5 ± 0.1	(0.16, 0.25)	880 ± 10	36 ± 2	280 ± 20
F2	Ag/BPyTP2 17 nm//DBR	6.3 ± 0.3	2.4 ± 0.2	(0.14, 0.18)	530 ± 20	160 ± 30	700 ± 50
C3	Al/BPyTP2 25 nm//ITO	9.9 ± 0.1	1.4 ± 0.1	(0.16, 0.27)	1,030 ± 10	50 ± 3	370 ± 15
F3	Ag/BPyTP2 25 nm//DBR	10.4 ± 0.5	2.0 ± 0.2	(0.15, 0.20)	800 ± 50	110 ± 20	430 ± 20

^aOnly variables in the top and bottom of the optical cavity are shown. See Extended Data Fig. 3 for detailed device structures.

^bThe natural PL quantum yield of the EML is $\eta_{PL,0} = 85 \pm 8\%$ (ref. 16) for Ir(cb)₃ and $44 \pm 1\%$ (ref. 11) for Ir(dmp)₃.

^cThe Purcell factors PF_{avg} are calculated by averaging across a triplet ensemble with isotropic dipole orientation: $PF_{avg} = 2/3PF_{horiz} + 1/3PF_{vert}$. Here PFs of horizontal and vertical dipoles are PF_{horiz} and PF_{vert}, respectively.

^dDevice lifetime data at constant current density are extracted from Fig. 4d.

PF decreases from $m = 2.4 \pm 0.3$ to $m = 1.7 \pm 0.3$, suggesting contributions from both TPA and TTA to ageing⁸. Apparently, extending device operational lifetime by increasing the radiative decay rate, k_r , is most effective early in the ageing process. As time progresses, triplets are decreasingly affected by the Purcell effect owing to increased fraction of nonradiative quenching by the rising population of defects (see equation (2) in Methods).

Figure 5b summarizes the device performance achieved by the polariton-enhanced Purcell effect, compared with that of the conventional Ir(dmp)₃ device C1 with the lowest PF. The enclosed triangular areas are proportional to the total number of equivalent deep-blue photons emitted throughout the device lifetime. Device F1 achieves the deepest blue colour and a 2.7 times increase from C1 in lifetime, while maintaining the same EQE as C1. Device F2 achieves the longest LT90, a 5.3 times increase from C1. However, the EQE is slightly reduced owing to the strong, competing energy transfer to PEPs. Device F3

has the highest EQE of $10.4 \pm 0.5\%$ and achieves a four times increase in LT90. Devices F1–F3 reach the best performance along each axis separately. Therefore, the introduction of PEPs in low-Q cavities markedly increases total deep-blue-photon output throughout the device lifetime while loosening the usual trade-off between device lifetime, colour and efficiency that characterizes conventional devices.

Figure 5c compares the normalized LT90 versus CIEy from this work with previously reported blue Ir-complex-based PHOLEDs (refs. 10–21). Here the normalized LT90 is calculated under a standard photon exitance $M_{p,0} = EQE \times J$, equivalent to a device with initial EQE of 25% aged at $J = 2 \text{ mA cm}^{-2}$, or an initial luminance $L_0 = 1,000 \text{ cd m}^{-2}$ for a cyan-emitting device with CIE = (0.17, 0.32) (see Extended Data Table 1 and Methods). A small CIEy coordinate is required for a blue pixel to reach the full-colour gamut in displays⁴, although the normalized LT90 shows an exponential decrease in the total number of outcoupled photons during the device lifetime with CIEy owing to a

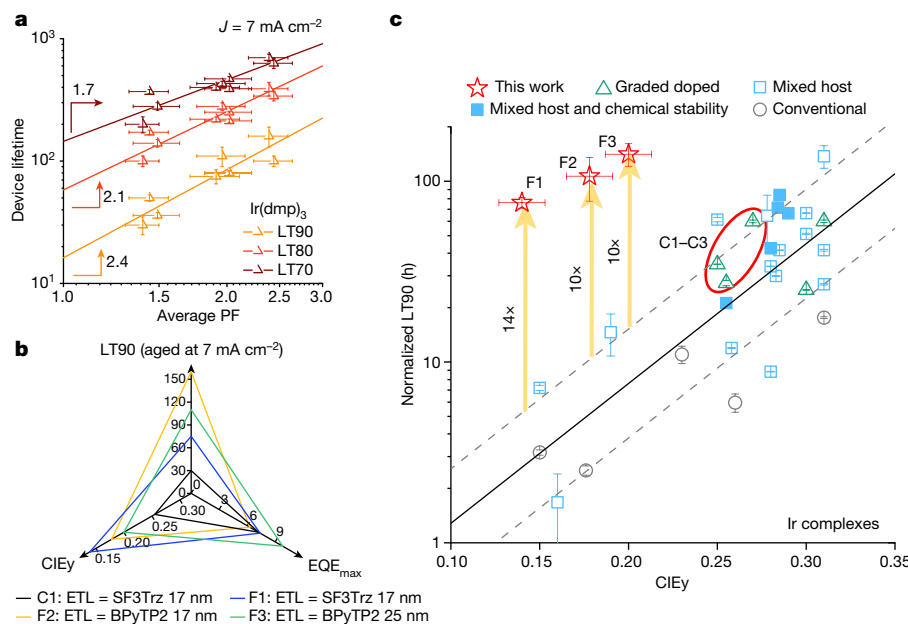


Fig. 5 | Ir(dmp)₃ device performance summary. **a**, Power law relating device operational lifetime to the calculated average PF for Ir(dmp)₃ devices C1–C3, H1–H3 and F1–F3. Three lifetime standards of LT90, LT80 and LT70 are shown at an ageing current density of 7 mA cm^{-2} with corresponding power laws of $m = 2.4 \pm 0.4$, $m = 2.1 \pm 0.3$ and $m = 1.7 \pm 0.3$. **b**, Comparison of LT90 at $J = 7 \text{ mA cm}^{-2}$, peak external quantum efficiency EQE_{max} and CIEy coordinates for C1 and F1–F3. **c**, Normalized LT90 versus CIEy of Ir-complex-based PHOLEDs reported for this work and from the literature^{10–21}. Devices F1–F3 are labelled by stars, gaining a

conservative 10–14 times increase in LT90 compared with devices with similar CIEy reported so far (vertical arrows). The conventional devices C1–C3 are labelled by triangles within the ellipse. Operational lifetimes are normalized to the photon exitance $M_{p,0} = EQE \times J$, equivalent to a device with EQE of 25% driven at $J = 2 \text{ mA cm}^{-2}$. An ageing acceleration factor of 1.8 ± 0.2 is adopted from the literature^{4,10,22} (see Methods for details). The solid black line shows the linear regression of the scattered data (except for the Purcell-enhanced devices in this work), with the upper and lower bounds denoted by dashed lines.

corresponding increase in exciton energy. As above, this results in a greater potential for excitons to engage in destructive bimolecular annihilation⁵. Thus, as commonly observed, deeper-blue devices have substantially shorter lives than cyan-emitting PHOLEDs, making the challenge of achieving adequate lifetimes for deep-blue devices increasingly more difficult.

Past demonstrations have reduced the effects of energetically driven degradation by means of spatial spreading of the triplet density profile by grading the EML doping^{10,11} or using mixed co-hosts in the EML (refs. 12,13,15–22), besides increasing chemical stability or steric hindrance to close packing^{13,22} of dopants and hosts to prevent their fragmentation. These efforts have increased the normalized LT90 from conventional, single-host, uniformly doped devices by one order of magnitude. On the basis of previous graded-doped devices^{10,11}, our method further achieves a threefold increase in LT90 and a shift of $\Delta\text{CIE}_y = -0.09 \pm 0.03$, representing a conservative estimated 14-fold improvement of F1 over similarly deep-blue Ir-based PHOLEDs. To our knowledge, F1 represents the longest-lived deep-blue PHOLED with $\text{CIE}_y < 0.15$ (refs. 10–20). Moreover, by tuning the PF and EQE of the Ag/BPyTP2PEP-enhanced Ir(dmp)₃ device F3 by adjusting the ETL thickness, we achieved a normalized LT90 = 140 ± 20 h with CIE = (0.15, 0.20), which is apparently the most stable blue Ir-based PHOLED reported so far^{10–21}.

Because the cavity design is independent of the host matrix and emitter composition, it can be applied to a variety of structures^{10–22} and other triplet-dominated devices, including those based on exciplex-forming co-host matrices^{12,13,15–22}. For example, a deep-blue, exciplex-forming co-host Ir(cb)₃ device¹⁶ achieved a 3.4 times device lifetime improvement compared with the control (see Extended Data Fig. 6b and Methods). Also, the fabrication of the bottom and top cavity structures are nonintrusive of the OLED layers while following standard OLED fabrication and general lithography processes. The solutions presented here for bottom emitting devices can equally be applied to top emitting PHOLEDs with suitable changes in the cavity structure.

In summary, we demonstrate that the Purcell effect in PHOLEDs is greatly enhanced by polaritons through PEPs, thereby markedly extending the operational lifetime of deep-blue devices while maintaining a high EQE. Polariton dispersion and cavity engineering provide new degrees of freedom for the design of OLEDs. For example, we achieved an average PF of 2.4 ± 0.2 through PEPs, leading to a maximum 5.3 times lifetime enhancement compared with analogous, conventional PHOLEDs. By introducing a weak cavity mode using a bottom DBR, we achieved a colour shift from cyan to deep blue for Purcell-enhanced Ir(dmp)₃ devices without decreasing the EQE or introducing noticeable angle dependence to the emission colour. Compared with similar devices with the same emission colour, we achieved a conservative estimate of 10–14 times increase in normalized LT90, which, to our knowledge, is the longest-lived blue Ir-based PHOLEDs yet reported. We demonstrate a 1.7–2.4 power-law dependence between the device operational lifetime and PF, showing the potential of this technique for substantially prolonging PHOLED lifetimes, particularly in the deep blue, as useful for both display and lighting applications.

Online content

Any methods, additional references, Nature Portfolio reporting summaries, source data, extended data, supplementary information, acknowledgements, peer review information; details of author contributions

and competing interests; and statements of data and code availability are available at <https://doi.org/10.1038/s41586-023-06976-8>.

1. Baldo, M. A. et al. Highly efficient phosphorescent emission from organic electroluminescent devices. *Nature* **395**, 151–154 (1998).
2. Adachi, C., Baldo, M. A., Thompson, M. E. & Forrest, S. R. Nearly 100% internal phosphorescence efficiency in an organic light emitting device. *J. Appl. Phys.* **90**, 5048–5051 (2001).
3. Universal PHOLED Product Data. <https://www.oled-info.com/files/UDC-Product-Sheets-sid-2011.pdf> (2011).
4. Forrest, S. R. *Organic Electronics: Foundations to Applications* (Oxford Univ. Press, 2020).
5. Giebink, N. C. et al. Intrinsic luminance loss in phosphorescent small-molecule organic light emitting devices due to bimolecular annihilation reactions. *J. Appl. Phys.* **103**, 044509 (2008).
6. Giebink, N. C., D’Andrade, B. W., Weaver, M. S., Brow, J. J. & Forrest, S. R. Direct evidence for degradation of polaron excited states in organic light emitting diodes. *J. Appl. Phys.* **105**, 124514 (2009).
7. Jeong, C. et al. Understanding molecular fragmentation in blue phosphorescent organic light-emitting devices. *Org. Electron.* **64**, 15–21 (2019).
8. Ha, D. G. et al. Dominance of exciton lifetime in the stability of phosphorescent dyes. *Adv. Opt. Mater.* **7**, 1901048 (2019).
9. Dintinger, J., Klein, S., Bustos, F., Barnes, W. L. & Ebbesen, T. W. Strong coupling between surface plasmon-polaritons and organic molecules in subwavelength hole arrays. *Phys. Rev. B* **71**, 035424 (2005).
10. Zhang, Y., Lee, J. & Forrest, S. R. Tenfold increase in the lifetime of blue phosphorescent organic light-emitting diodes. *Nat. Commun.* **5**, 5008 (2014).
11. Lee, J. et al. Hot excited state management for long-lived blue phosphorescent organic light-emitting diodes. *Nat. Commun.* **8**, 15566 (2017).
12. Kim, S. et al. Degradation of blue-phosphorescent organic light-emitting devices involves exciton-induced generation of polaron pair within emitting layers. *Nat. Commun.* **9**, 1211 (2018).
13. Bae, H. J. Protecting benzylic C–H bonds by deuteration doubles the operational lifetime of deep-blue Ir-phenylimidazole dopants in phosphorescent OLEDs. *Adv. Opt. Mater.* **9**, 2100630 (2021).
14. Sim, B. et al. Comprehensive model of the degradation of organic light-emitting diodes and application for efficient, stable blue phosphorescent devices with reduced influence of polarons. *Phys. Rev. Appl.* **14**, 024002 (2020).
15. Yang, K. et al. Effects of charge dynamics in the emission layer on the operational lifetimes of blue phosphorescent organic light-emitting diodes. *Adv. Funct. Mater.* **32**, 2108595 (2022).
16. Zhao, H. et al. Control of host-matrix morphology enables efficient deep-blue organic light-emitting devices. *Adv. Mater.* **35**, 2210794 (2023).
17. Ihn, S. G. et al. Cohosts with efficient host-to-emitter energy transfer for stable blue phosphorescent organic light-emitting diodes. *J. Mater. Chem. C* **9**, 17412–17418 (2021).
18. Choi, K. H., Lee, K. H., Lee, J. Y. & Kim, T. Simultaneous achievement of high efficiency and long lifetime in deep blue phosphorescent organic light-emitting diodes. *Adv. Opt. Mater.* **7**, 1901374 (2019).
19. Shin, S. K., Han, S. H. & Lee, J. Y. High triplet energy exciplex host derived from a CN modified carbazole based n-type host for improved efficiency and lifetime in blue phosphorescent organic light-emitting diodes. *J. Mater. Chem. C* **6**, 10308–10314 (2018).
20. Kim, J. S. et al. Improved efficiency and stability of blue phosphorescent organic light emitting diodes by enhanced orientation of homoleptic cyclometalated Ir(III) complexes. *Adv. Opt. Mater.* **8**, 2001103 (2020).
21. Jung, M., Lee, K. H., Lee, J. Y. & Kim, T. A bipolar host based high triplet energy electroplex for an over 10000 h lifetime in pure blue phosphorescent organic light-emitting diodes. *Mater. Horiz.* **7**, 559–565 (2020).
22. Sun, J. et al. Exceptionally stable blue phosphorescent organic light-emitting diodes. *Nat. Photonics* **16**, 212–218 (2022).
23. Bulović, V., Khalfin, V., Gu, G., Burrows, P. & Garbuzov, D. Weak microcavity effects in organic light-emitting devices. *Phys. Rev. B* **58**, 3730–3740 (1998).
24. Fusella, M. A. et al. Plasmonic enhancement of stability and brightness in organic light-emitting devices. *Nature* **585**, 379–382 (2020).
25. Zengin, G. et al. Realizing strong light-matter interactions between single-nanoparticle plasmons and molecular excitons at ambient conditions. *Phys. Rev. Lett.* **114**, 157401 (2015).
26. Deng, H., Haug, H. & Yamamoto, Y. Exciton-polariton Bose-Einstein condensation. *Rev. Mod. Phys.* **82**, 1489–1537 (2010).

Publisher’s note Springer Nature remains neutral with regard to jurisdictional claims in published maps and institutional affiliations.

Springer Nature or its licensor (e.g. a society or other partner) holds exclusive rights to this article under a publishing agreement with the author(s) or other rightsholder(s); author self-archiving of the accepted manuscript version of this article is solely governed by the terms of such publishing agreement and applicable law.

© The Author(s), under exclusive licence to Springer Nature Limited 2023

Methods

Polariton-enhanced Purcell effect

Strong light–matter interactions of polaritons increase the total ODoS by introducing an anticrossing between the ETL singlet exciton energy and the resonant optical modes. The anticrossing shifts the polariton dispersion to be resonant with blue triplet emission. According to Fermi’s golden rule, the triplet radiative decay rate is:

$$k_r = \frac{2\pi}{\hbar} \sum_{\hbar\omega_0, \mathbf{p}} |\hat{\mu}_{\omega_0, \mathbf{p}}|^2 \rho_p(\mathbf{r}_0, \omega_0). \quad (1)$$

Here $\hat{\mu}_{\omega_0, \mathbf{p}}$ and \hbar are the triplet transition dipole moment matrix element and the reduced Planck’s constant, respectively. The triplets transfer energy to the polaritons in the weak-coupling regime owing to their low oscillator strength, which is proportional to $|\hat{\mu}_{\omega_0, \mathbf{p}}|^2$. In the weak-coupling regime, the PF is proportional to the ODoS. For planar OLEDs, the ODoS is determined by the dyadic Green’s function $\mathbf{G}(\mathbf{r}_0, \mathbf{r}_0; \omega_0)$ by $\rho_p(\mathbf{r}_0, \omega_0) \propto \mathbf{n}_p \cdot \text{Im}[\mathbf{G}(\mathbf{r}_0, \mathbf{r}_0; \omega_0)] \cdot \mathbf{n}_p \propto \sum_{\mathbf{k}} |\mathbf{u}_{\mathbf{k}, \mathbf{p}}|^2 \delta(\omega_k - \omega_0)$ (ref. 27), which is a function of the dispersion relation, ω_k , for multimode expansion $\mathbf{u}_{\mathbf{k}, \mathbf{p}}$ with modal wavevector, \mathbf{k} , and dipole orientation, \mathbf{p} (horizontal or vertical in cylindrical coordinates, depicted by the unit vector \mathbf{n}_p). The PEPs and Ag-enhanced SPPs have a larger mode density $|\mathbf{u}_{\mathbf{k}, \mathbf{p}}|^2$ integrating over the high- k_x region. The PF is primarily controlled by the energy transfer rate to the polaritons at the metal–ETL interface. The PEP results from the coupling of excitons in the ETL with SPPs on the metal cathode; ETLs such as BPYTP2, with a large extinction coefficient of 0.95 ± 0.05 at a wavelength of $\lambda = 345$ nm and an energy gap of 3.0 eV (ref. 28). This results in strongly coupled PEPs with Ag or Al plasmon modes (see Fig. 2 and Extended Data Fig. 2). Compared with the conventional Al cathode, Ag has an absorption band starting from 3.8 eV (ref. 29) that leads to the flattening of the high- k_x plasmon modes.

The Purcell effect prolongs the device operational lifetime by reducing the triplet density, thus slowing defect generation (and, hence, nonradiative quenching) through TPA and TTA. Device degradation is a function of the decreasing PL quantum yield, η_{PL} (refs. 4,5,8):

$$\eta_{PL}(t) = \frac{k_r}{k_{tot}} = \frac{\text{PF} k_{r0}}{\text{PF} k_{r0} + k_{nr} + K_{QN} Q(t)} \quad (2)$$

$$\frac{dQ(t)}{dt} = K_{TPA} N(t) n(t) + K_{TTA} N(t)^2 + \text{etc..} \quad (3)$$

Here k_{tot} , k_{nr} , K_{TPA} , K_{TTA} and K_{QN} are the total decay rate, the natural nonradiative decay rate, the defect generation rates owing to TPA and TTA and the bimolecular quenching rate between the triplets of density N and the defects of density Q , respectively. For a phosphor with $\eta_{PL} \approx 100\%$, the Purcell effect reduces the initial triplet density by $1/\text{PF}$. This, in turn, reduces the initial rate of defect generation induced by TPA or TTA by $1/\text{PF}$ or $1/\text{PF}^2$, respectively^{4,5,8}. Moreover, for the same η_{PL} loss, a larger defect density is required to match the increased radiative decay rates equivalent to that required before ageing. The slowed defect generation and reduced quenching give rise to a power law $m > 1$ between the lifetime enhancement and PF in equations (2) and (3).

In an OLED, vertical dipoles only excite TM modes and thus are inefficiently outcoupled³⁰, whereas the horizontal (in-plane) dipoles couple to both transverse electric (TE) and TM modes. Because PEPs and SPPs are TM-polarized, the vertical dipoles share a higher PF than horizontal dipoles, with a local maximum of $\text{PF} = 7.5$ nearest to the cathode (see Extended Data Fig. 4b). As a result, the TM-polariton-enhanced Purcell effect reduces the probability of annihilation of inefficiently outcoupled triplets with vertical-transition dipole moments.

This is consistent with TrPL measurements in Fig. 3b and Extended Data Fig. 4c. With increasing TM-polariton energy transfer, the contrast in PF between vertical and horizontal dipoles diverges, such that the

outcoupled PL signal is eventually dominated by horizontal dipoles. To estimate the actual PF, we calculate its value assuming isotropic dipoles averaged over the 50-nm-thick EML.

The measured PL transients in Fig. 3b show a negligible change in low- Q Ag/DBR cavities. This is consistent with the dominance of the polariton ODoS among outcoupled, substrate and waveguided modes in Extended Data Fig. 4a. Owing to the near-field nature of surface modes, the average PF is primarily controlled by the ETL thickness.

Design and modelling of the PEPs and SPPs

The ETL is chosen for its large oscillator strength at wavelengths slightly shorter than the triplet emission wavelength. Therefore, the LP branch of the PEP is redshifted from the bare SPP owing to its anticrossing behaviour. The dispersion and ODoS are tuned by the thickness of the ETL using transfer matrix and Green’s function simulations^{31,32}. A higher ETL exciton energy than the dopant triplet energy prevents exciton leakage through Förster or Dexter energy transfer from the triplets, which reduces PHOLED efficiency. However, an ETL exciton energy close to the triplet energy increases the overlap between the PEP LP dispersion and the triplet emission spectra, leading to a large ODoS at the emission wavelengths. Therefore, an efficient ETL exciton with large oscillator strength at wavelengths slightly shorter than the triplet emission wavelength is optimal for exciting PEP-enhanced Purcell effects.

In Fig. 2a, the PEP of a 20-nm Al/20-nm BPYTP2 bilayer is identified by angle-dependent reflectance spectroscopy. The measured Al/BPYTP2 PEP dispersions are extracted from the local minima with the linear background subtracted in Extended Data Fig. 2 and fit to the coupled oscillator model:

$$\hat{H}(k_x/k_0) = \begin{pmatrix} E_{SPP} & g_1 & g_2 & g_3 \\ g_1 & E_{ex1} & 0 & 0 \\ g_2 & 0 & E_{ex2} & 0 \\ g_3 & 0 & 0 & E_{ex3} \end{pmatrix} \quad (4)$$

Here E_{SPP} is the bare SPP dispersion and g_1 , g_2 and g_3 are the coupling strengths between the SPP mode and BPYTP2 0-0, 0-1 and 0-2 exciton vibronic states, respectively. The strongly coupled PEP is identified by the anticrossing between the bare SPP dispersion and the exciton, with a Rabi splitting energy of $\Omega_i = \sqrt{4g_i^2 - (\Gamma_{ex,i} - \Gamma_{SPP})^2}$, ($i = 1, 2, 3$) (ref. 33), which is larger than the linewidths of the SPP mode and the exciton ($\Gamma_{SPP} + \Gamma_{ex,i}$). Here g_1 and g_2 obtained from the spectral fits are 0.64 ± 0.05 eV and 0.70 ± 0.05 eV, respectively. The linewidths extracted from the extinction coefficients and SPP angle-resolved reflection measurements are $\Gamma_{ex,0-0} = 0.48 \pm 0.01$ eV, $\Gamma_{ex,0-1} = 0.50 \pm 0.01$ eV and $\Gamma_{SPP} = 0.3 \pm 0.1$ eV. The Rabi splitting energies for the 0-0 and 0-1 excitons are 1.3 ± 0.1 eV and 1.4 ± 0.1 eV, respectively, confirming that the strong-coupling regime is reached.

Ir(cb)₃ device performance

Operational-lifetime improvements have also been found for PHOLEDs using the deep blue but relatively short-lived phosphor, Ir(cb)₃, in a mixed co-host mCBP:SiTrzCz2 EML (ref. 16) (see Extended Data Table 1 and Extended Data Fig. 6b for detailed lifetime data). Ir(cb)₃ devices C4–C6 feature Al/BPYTP2 PEPs, whereas H5 and H6 interact with Ag/BPYTP2 PEPs. All Ir(cb)₃ devices are aged at $J = 5 \text{ mA cm}^{-2}$. Among Ir(cb)₃ devices, structures 4–6 use a BPYTP2 ETL with thicknesses reduced from 40 nm to 15 nm for enhanced energy transfer to the PEPs. Increasing the near-field energy transfer to the Al/BPYTP2 PEP by reducing the ETL thickness doubles the device lifetime from C4 to C5 and C6. By contrast, when the ETL thickness is reduced from 20 nm to 15 nm and the PF is increased from 2.1 ± 0.2 to 2.4 ± 0.2 for H5 to H6, the operational lifetime is increased from 2.1 ± 0.1 to 3.4 ± 0.1 times compared with C4. The similar device lifetimes of C5 and H5 with different PFs may be because of other factors introduced to the Ir(cb)₃ devices by changing

the cathode. Nevertheless, the Purcell effect enhanced by Ag/BPyTP2 PEPs in H6 still greatly prolongs the device lifetime. Compared with the lifetime enhancement, the EQE only shows a moderate decrease for H5 and H6 owing to energy transfer to Ag/BPyTP2 PEP, whereas the emission colour is saturated with a shift of $\Delta\text{CIEy} = -0.1$ (see Extended Data Fig. 6c,d and Extended Data Table 1). The current–voltage characteristics show no change (see Extended Data Fig. 6e).

Device fabrication

PHOLEDs are grown on glass substrates with pre-patterned bottom electrodes that are solvent-cleaned and treated by UV-ozone plasma for 15 min. For full-cavity devices, the DBRs are grown by plasma-enhanced chemical vapour deposition at a temperature of 200 °C. The 50–60-nm-thick ITO layer is deposited by magnetron sputtering in an Ar plasma with a partial pressure of 2 mTorr at a deposition rate of 1.5 Å s⁻¹. The thickness and number of pairs of the DBR are iterated to match the linewidth and spectral overlap of the phosphor emission spectrum. The SiN_x/SiO₂ layer thicknesses are 56 nm/80 nm targeted at a central wavelength of 465 nm, with 10% variation from batch to batch. The thicknesses of the ITO and SiN_x capping layers are iterated to align the cavity modes with the phosphor emission spectrum. The ITO is rapid thermal annealed at 450 °C under forming gas for 3 min (20–40 Ω sq⁻¹). The ITO is wet-etched in HCl:H₂O (1:1 volume ratio) for 16 min, with the electrode pattern protected by 3-μm-thick S1813 photoresist. The organic layers are deposited by thermal evaporation in a vacuum chamber with a base pressure <10⁻⁷ torr.

The materials used, some of which are shown in Extended Data Fig. 1, are: (1) 2-(9,9'-spirobi[fluoren]-3-yl)-4,6-diphenyl-1,3,5-triazine (SF3Trz) 17 nm/3,3'-di(9H-carbazol-9-yl)-1,1'-biphenyl (mCBP) 5 nm/mCBP: iridium (III) tris[3-(2,6-dimethylphenyl)-7-methylimidazo[1,2-f]phenanthridine] (Ir(dmp)₃) 18–8 vol% graded/N,N'-di(1-naphthyl)-N,N'-diphenyl-(1,1'-biphenyl)-4,4'-diamine (NPD) + dipyrrazino[2,3-f:2',3'-h]quinoxaline-2,3,6,7,10,11-hexacarbonitrile (HATCN) 10 nm; (2) 2,7-di(2,2'-bipyridin-5-yl)triphenylene (BPyTP2) 17 nm/mCBP 5 nm/mCBP: Ir(dmp)₃ 18–8 vol% graded/NPD + HATCN 10 nm; (3) BPyTP2 25 nm/mCBP 5 nm/mCBP: Ir(dmp)₃ 18–8 vol% graded/NPD + HATCN 10 nm; (4) BPyTP2 40 nm/9,9'-(6-(3-(triphenylsilyl)phenyl)-1,3,5-triazine-2,4-diyl) bis(9H-carbazole) (SiTrzCz2) 5 nm/mCBP: SiTrzCz2: fac-tris(5-(tert-butyl)-1,3-diphenyl2,3-dihydro-1H-imidazo[4,5-b]pyrazine)iridium] (Ir(cb)₃) (40:40:20 vol%) 50 nm/mCBP 5 nm/NPD 5 nm/HATCN 5 nm; (5) BPyTP2 20 nm/SiTrzCz2 5 nm/mCBP: SiTrzCz2: Ir(cb)₃ (40:40:20 vol%) 50 nm/mCBP 5 nm/NPD 5 nm/HATCN 5 nm; (6) BPyTP2 15 nm/SiTrzCz2 5 nm/mCBP: SiTrzCz2: Ir(cb)₃ (40:40:20 vol%) 50 nm/mCBP 5 nm/NPD 5 nm/HATCN 5 nm.

The cathodes are deposited using a thin metal shadow mask to define the 2-mm² device active area. All Al layers are deposited first at a rate of 0.1 Å s⁻¹ up to a thickness of 50 Å and then at 1 Å s⁻¹ until 100 nm total thickness is reached. All Ag layers are deposited at a rate of 0.1 Å s⁻¹ up to a thickness of 150 Å and then at 0.6 Å s⁻¹ until 100 nm total thickness is reached. The devices are encapsulated by a glass cover attached to the substrate using a bead of UV-cured epoxy around its periphery in a N₂ environment with O₂/H₂O concentrations <0.1 ppm.

Device characterization

(1) Current–voltage (I – V) and EQE characterization

The I – V , luminance and EQE characteristics are measured using a semiconductor parameter analyser (B1500A, Keysight Technologies) and a calibrated, large-area photodiode (S3584-08, Hamamatsu Photonics) collecting all photons in the forward-viewing direction following standard procedures³⁴ to eliminate errors owing to the angular dependence of emission. The electroluminescence (EL) spectra are measured using a fibre-coupled spectrometer (USB4000, Ocean Optics, Inc.). The EQE data are taken from at least two different batches and at least two devices in each batch.

(2) Device operational lifetime characterization

Device operational lifetime is measured at a constant current density and room temperature. The luminance data are collected using automated source-measurement units (Agilent, U2722 and Agilent, 34972A). Lifetime data are taken from at least two different batches and at least two devices.

Operational lifetime of Ir(dmp)₃ and Ir(cb)₃ devices are fitted to the stretched exponential model: $L(t)/L_0 = \exp[-(t/t_0)^\beta]$. The fitting parameters t_0 and β are listed in Extended Data Table 2.

(3) Operational lifetime normalized to initial photon exitance, $M_{p,0}$

To compare PHOLEDs using different phosphors, emission spectra and device structures in the literature, we normalize device operational lifetime data to an empirical acceleration model⁴:

$$\text{LTx}(M_{p,0}) = \text{LTx}(M_{p,\text{test}}) \cdot \left[\frac{M_{p,\text{test}}}{M_{p,0}} \right]^n \quad (5)$$

Here $M_p = \text{EQE} \times J$ is the initial photon exitance of the device and n is the acceleration factor. $M_{p,\text{test}}$ is the initial photon exitance at the test condition and $M_{p,0}$ is the initial photon exitance close to the mean of the reference data. We adopt an acceleration factor $n = 1.8 \pm 0.2$ following the literature^{4,10,22}.

Given the same phosphor and emission spectra, the luminance of the device is directly proportional to the photon exitance. Therefore, normalizing to the initial photon exitance provides the bridge between the energy-based, physical degradation process and the usual photometric standard. In this study, we normalize all lifetime data to $M_{p,0} = 25\% \times 2 \text{ mA cm}^{-2}$, equivalent to a PHOLED with EQE of 25% aged at 2 mA cm⁻². For a cyan-emitting device with CIEy ≈ 0.30 (refs. 13,20), this corresponds to an initial luminance of $L_0 = 1,000 \text{ cd m}^{-2}$.

Optical characterization

(1) TrPL

The TrPL measurements use a 50-nm-thick mCBP:SiTrzCz2:Ir(cb)₃ (40:40:20 vol%) EML owing to its high η_{PL} of 85 ± 8% (ref. 16). The optical structures are: 100 nm metal/x nm ETL/5 nm SiTrzCz2/50 nm mCBP: SiTrzCz2:Ir(cb)₃ (40:40:20 vol%)/5 nm mCBP/10 nm HATCN/50 nm ITO or 50–60 nm ITO/DBR (15 nm SiN_x/80 nm SiO₂/56 nm SiN_x/80 nm SiO₂/56 nm SiN_x).

The TrPL data for the full device structures are collected using a time-correlated single-photon counter (PicoHarp 300, PicoQuant) coupled to a microscope (Eclipse Ti2, Nikon). The pump laser (P-C-405, PicoQuant) wavelength is 405 nm, with a repetition rate of 10 kHz, a pump power <1 nW and a beam diameter of 0.5 μm. The pump wavelength is selected to reach the maximum ratio of the phosphor-to-background emission in other organic layers, such as BPyTP2. After the prompt emission, the slowly decaying TrPL data are fitted using:

$$\frac{dN}{N_0 dt} = \frac{1}{\tau} \frac{N}{N_0} + K_{\text{TT}} \left(\frac{N}{N_0} \right)^2 \quad (6)$$

Here τ , K_{TT} and N_0 are the PL lifetime of the phosphor, triplet–triplet quenching rate and the initial triplet density, respectively. The pump power is selected such that $\tau K_{\text{TT}} N_0 \ll 10\%$ to avoid the effects of the bimolecular quenching.

(2) Angle-resolved reflection and PL spectra

Angle-resolved reflectance is measured using ellipsometry (Woolam 2000, Woolam). The structures for Fig. 2 are: ETL 20 nm/Al 20 nm and ETL 20 nm/Ag 40 nm on a UV-fused silica prism coupler. The transfer matrix method³³ is used to model the angle-resolved reflection of the multilayer structures.

The angle-resolved PL spectra in Figs. 2c and 4c are obtained using an oil-immersion objective (×100, NA = 1.40, Olympus) and a 4f Fourier imaging system ($f = 200 \text{ mm}$). The Fourier image of the

Article

reflection and PL signal passes through an analyser, reconstructed on the charge-coupled device (PIXIS 1024B, Teledyne Princeton Instruments) and resolved by a spectrograph (HRS500, Teledyne Princeton Instruments)³³. All angle-resolved PL spectra in Fig. 2c are pumped by a 405-nm wavelength, 1-kHz ns-pulsed laser with a fluence of 1 J cm^{-2} and integrated for 1 min. The signal is filtered by a 425-nm long-pass filter placed before the monochromator.

(3) Ellipsometry and n - k measurements

Optical constants are measured from 250 to 1,700 nm using an ellipsometer (Woollam 2000, Woollam) and averaged over several thin films (20–50 nm) on Si/SiO₂ substrates fitted to B-spline and general oscillator models. The extinction coefficient, k , is iterated by comparing it with the UV-visible spectra (Perkin Elmer 1050) of the same thin films on sapphire substrates.

Dyadic Green's function simulation

The dyadic Green's function method follows Celebi et al.³¹ based on a dipole embedded in a multilayer structure³². The OLED structure determines the multimode expansion of the Green's function and, thereby, the electrical field and ODoS. The dissipated power, simulated by taking the real part of the Poynting vector, is proportional to the decay rate of the dipole and thus is proportional to the ODoS (ref. 27). On the basis of the in-plane wavevector k_x/k_0 , the optical modes are outcoupled modes (including outcoupled cavity modes), substrate modes, waveguide modes and SPP/PEP modes, among others⁴. Therefore, the PF and energy transfer rates are calculated through the ODoS and dissipated radiative power of each mode. The PF is the total ODoS, $\rho_{\text{tot}}(\omega_k)$, of a dipole normalized by that of a dipole in an isotropic, infinite medium of the EML. The outcoupling efficiency is calculated from the dissipated power through modes with $k_x/k_0 < 1$ normalized to the total ODoS, $\rho_{\text{tot}}(\omega_k)$. The average PF of each device is calculated from the overlap of the emission spectra of Ir(dmp)₃ and a uniform exciton spatial distribution (see Extended Data Fig. 4b,c), assuming isotropic dipole orientation. The energy transfer rates of each dissipation channel in Fig. 3a are calculated from measured EQE, PL quantum yield and EL spectra and the calculated average PF, for which the ratio of natural radiative and natural nonradiative decay rates is $k_{r,0}:k_{nr} = \eta_{PL}:1 - \eta_{PL}$, outcoupling efficiency is $\eta_{\text{out}} = \text{EQE}_{\text{max}}/\text{PL quantum yield}$ assuming perfect charge balance, outcoupled and high- k_x radiative channel coupling rates are $k_{r,\text{out}} = \text{PF} \times \eta_{\text{out}}$ and $k_{r,\text{high}} = \text{PF} \times (1 - \eta_{\text{out}})$, respectively.

Data availability

The data that support the findings of this study are available from the corresponding author on request.

27. Novotny, L. & Hecht, B. *Principles of Nano-Optics* (Cambridge Univ. Press, 2012).
28. Togashi, K., Nomura, S., Yokoyama, N., Yasuda, T. & Adachi, C. Low driving voltage characteristics of triphenylene derivatives as electron transport materials in organic light-emitting diodes. *J. Mater. Chem.* **22**, 20689–20695 (2012).
29. Yang, H. U. et al. Optical dielectric function of silver. *Phys. Rev. B* **91**, 235137 (2015).
30. Kim, S. Y. et al. Organic light-emitting diodes with 30% external quantum efficiency based on a horizontally oriented emitter. *Adv. Funct. Mater.* **23**, 3896–3900 (2013).
31. Celebi, K., Heidel, T. D. & Baldo, M. A. Simplified calculation of dipole energy transport in a multilayer stack using dyadic Green's functions. *Opt. Express* **15**, 1762 (2007).
32. Chance, R. R., Prock, A. & Silbey, R. Molecular fluorescence and energy transfer near interfaces. *Adv. Chem. Phys.* **37**, 1–65 (2007).
33. Hou, S., Qu, Y., Liu, X. & Forrest, S. R. Ultrastrong coupling of vibrationally dressed organic Frenkel excitons with Bloch surface waves in a one-sided all-dielectric structure. *Phys. Rev. B* **100**, 045410 (2019).
34. Forrest, S. R., Bradley, D. D. C. & Thompson, M. E. Measuring the efficiency of organic light-emitting devices. *Adv. Mater.* **15**, 1043–1048 (2003).

Acknowledgements We thank J.-Y. Lee from Sungkyunkwan University for providing SiTrzCz2 and Ir(cb)₃ and J. Kim from Yonsei University for helpful discussions. This material is based on work partially supported by the U.S. Department of Energy's Office of Energy Efficiency and Renewable Energy (EERE) under award number DE-EE00009688. This report was prepared as an account of work sponsored by an agency of the United States Government. Neither the United States Government nor any agency thereof, nor any of their employees, makes any warranty, expressed or implied, or assumes any legal liability or responsibility for the accuracy, completeness or usefulness of any information, apparatus, product or process disclosed, or represents that its use would not infringe privately owned rights. Reference herein to any specific commercial product, process or service by trade name, trademark, manufacturer or otherwise does not necessarily constitute or imply its endorsement, recommendation or favouring by the United States Government or any agency thereof. The views and opinions of the authors expressed herein do not necessarily state or reflect those of the United States Government or any agency thereof. We also thank Universal Display Corp. for partial financial support of this research.

Author contributions H.Z. planned the experiments, built the experimental setup and conducted the experiments and simulations. D.F. helped with fabrication. C.E.A. helped with obtaining the optical data. S.R.F. planned and supervised the project and analysed the data. All authors contributed to the preparation of the manuscript and analysed the data.

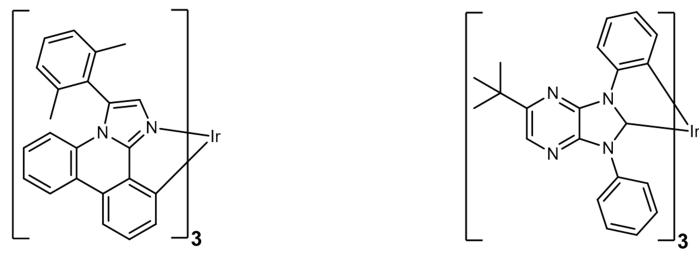
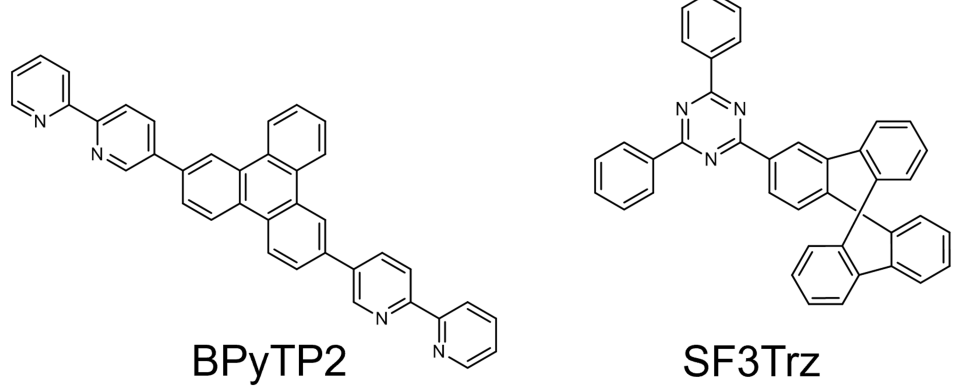
Competing interests S.R.F. has an equity interest in Universal Display Corp. This apparent conflict is under management by the University of Michigan Office of Research. Also, the University of Michigan has a royalty-bearing license agreement with Universal Display Corp.

Additional information

Correspondence and requests for materials should be addressed to Stephen R. Forrest.

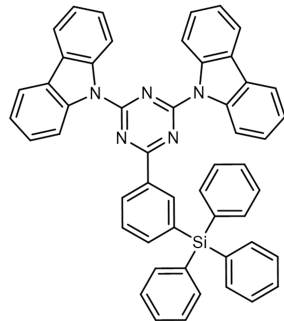
Peer review information *Nature* thanks the anonymous reviewers for their contribution to the peer review of this work.

Reprints and permissions information is available at <http://www.nature.com/reprints>.



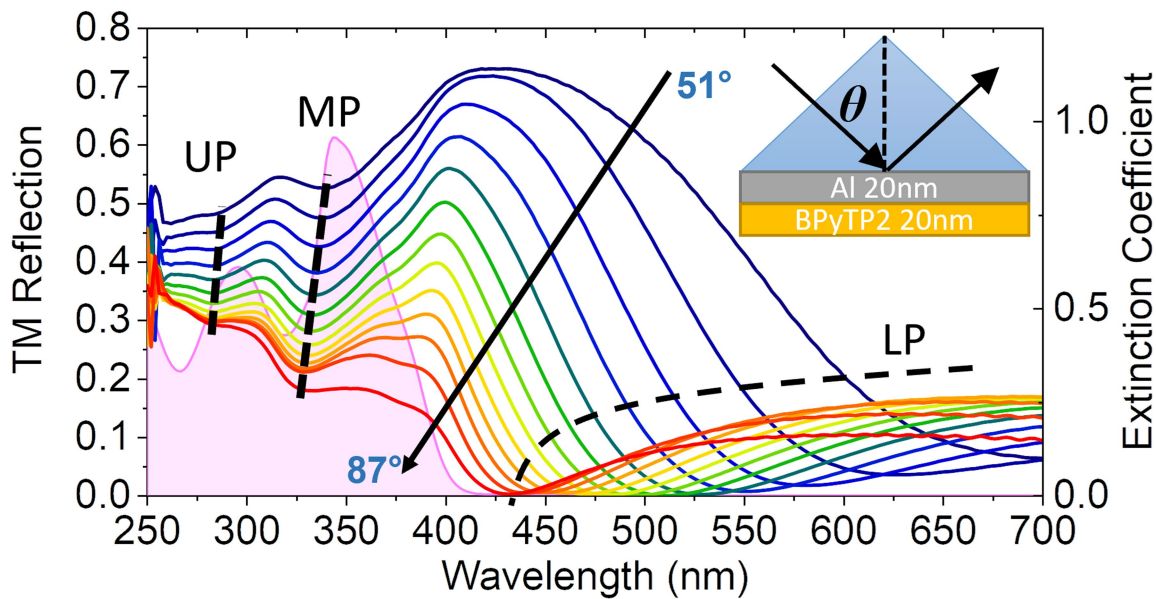
Ir(dmp)₃

Ir(cb)₃



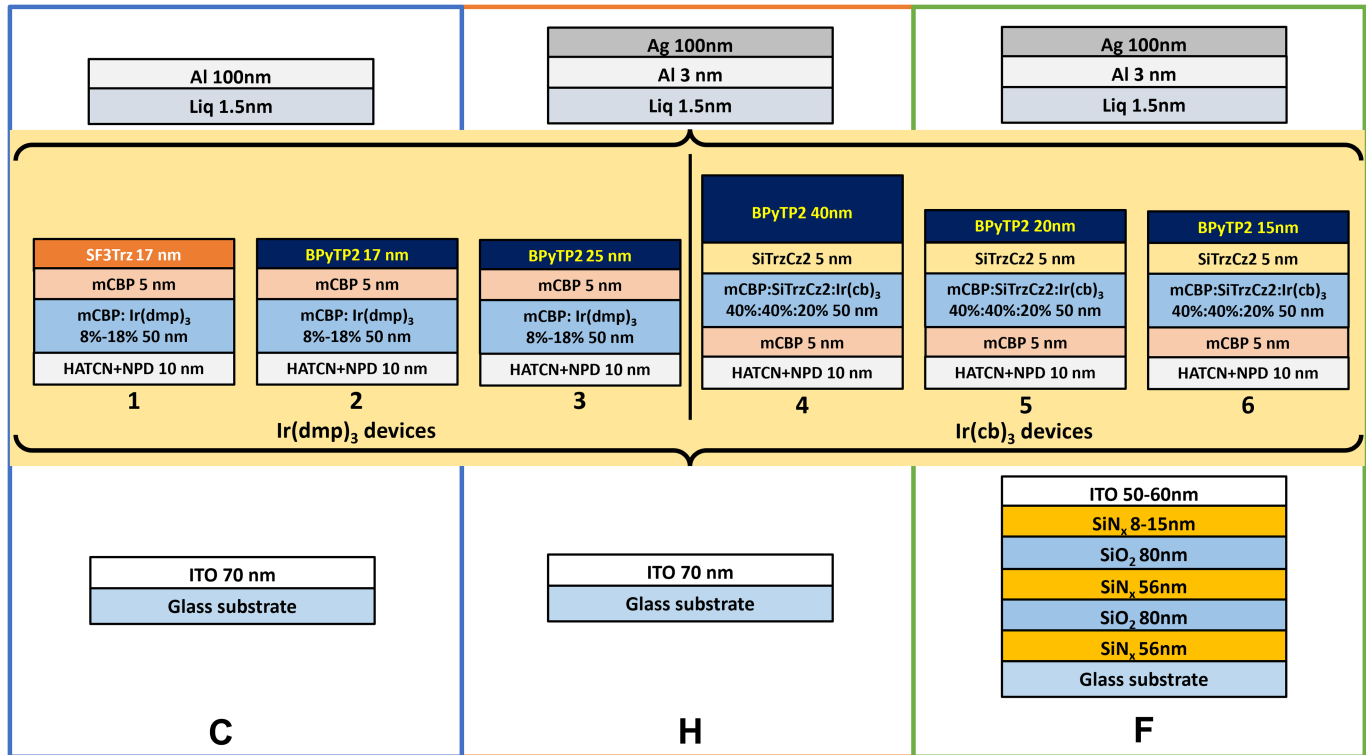
SiTrzCz2

Extended Data Fig. 1 | Molecular structural formulae of organic materials used in the EML, ETL and hosts. The molecules are all deposited from vacuum along with other molecules forming the complete OLED structures, whose complete chemical nomenclatures are provided in Methods.

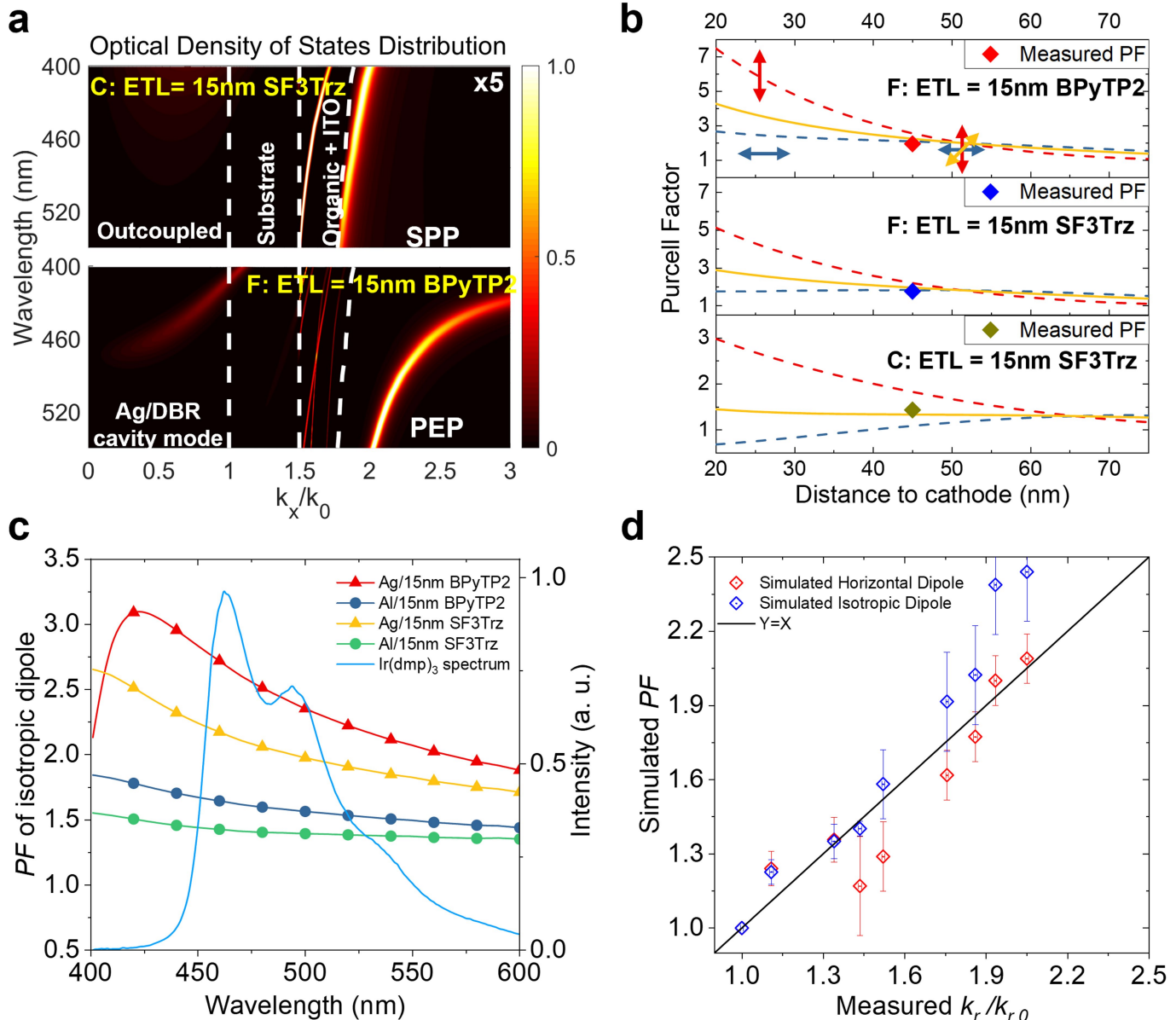
**Extended Data Fig. 2 | Angle-resolved TM-mode reflectance of Al/BPyTP2.**

The measurement angles are increased from $\theta = 51^\circ$ to 87° by 3° increments, indicated by solid lines. The dashed black lines provide guides to the dispersion of LP, MP and UP branches. The extinction coefficient of BPyTP2 is shown by the

filled pink area. The PEP dispersion in Fig. 2a is fitted to the local minima. Inset, ellipsometry measurement setup. 20-nm-thick Al/20 nm BPyTP2 is coated on a prism coupler.

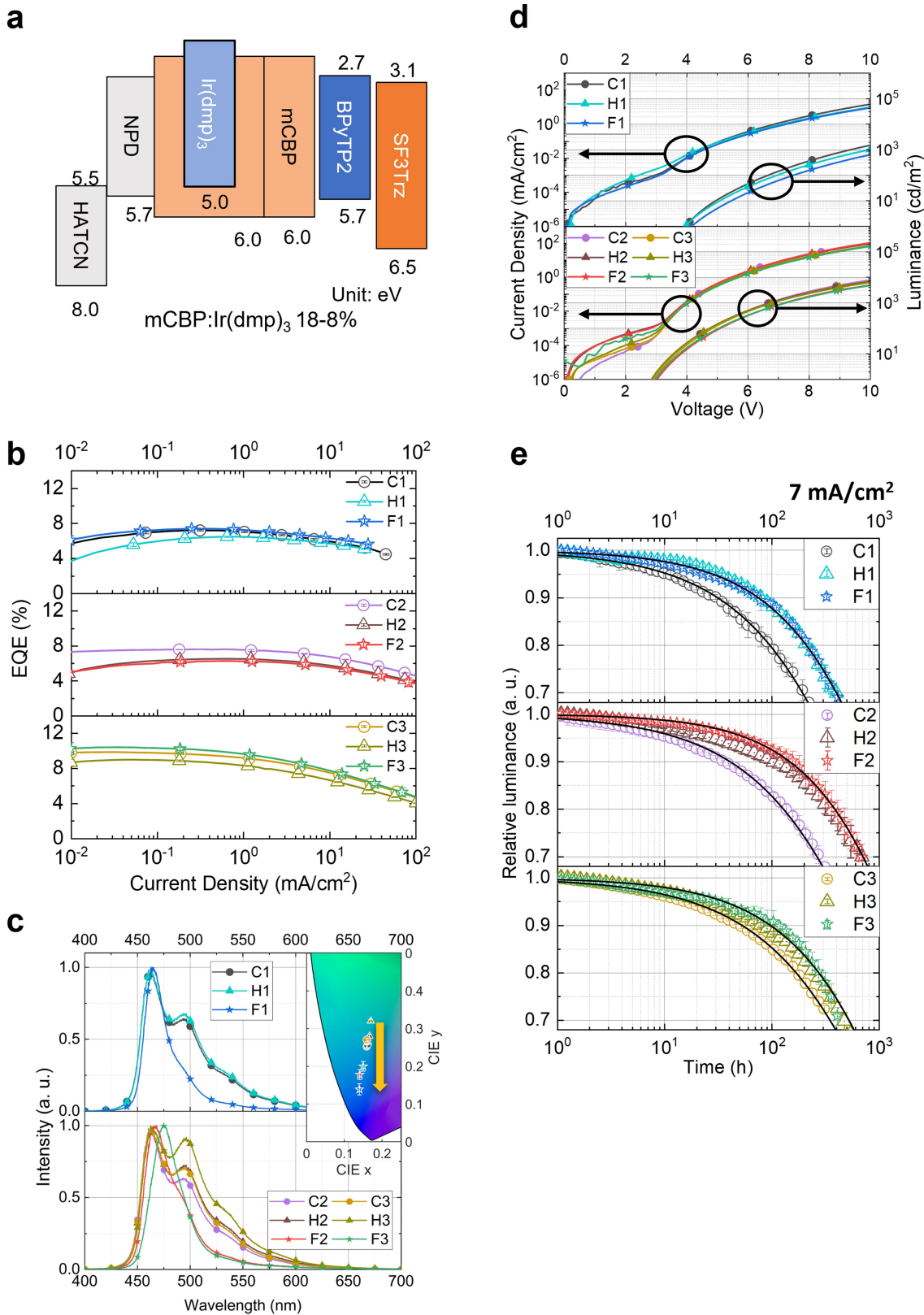


Extended Data Fig. 3 | Device structures used in this study. C, H and F label the cathode and anode structures and 1–6 label the organic structures sandwiched between the electrodes.



Extended Data Fig. 4 | Simulated and measured PFs for the devices studied. **a**, ODoS distribution simulated using dyadic Green's functions^{31,32} for structure C with a 15-nm-thick SF3Trz ETL and structure F with a 15-nm-thick BPYTP2 ETL. The triplet dipole position is in the middle of the EML with an isotropic orientation relative to the film plane. Dashed white lines separate regions of different optical modes. Structure F has a low- Q Ag/DBR cavity mode at $k_x/k_0 < 1$. The relative ODoS intensity is labelled by the colour bar on the right. The ODoS for structure C is multiplied by five for comparison. **b**, Simulated PF versus triplet emitter position for structures C and F for different cathode/ETL combinations. The horizontal and vertical dipoles are labelled by dash blue and red lines,

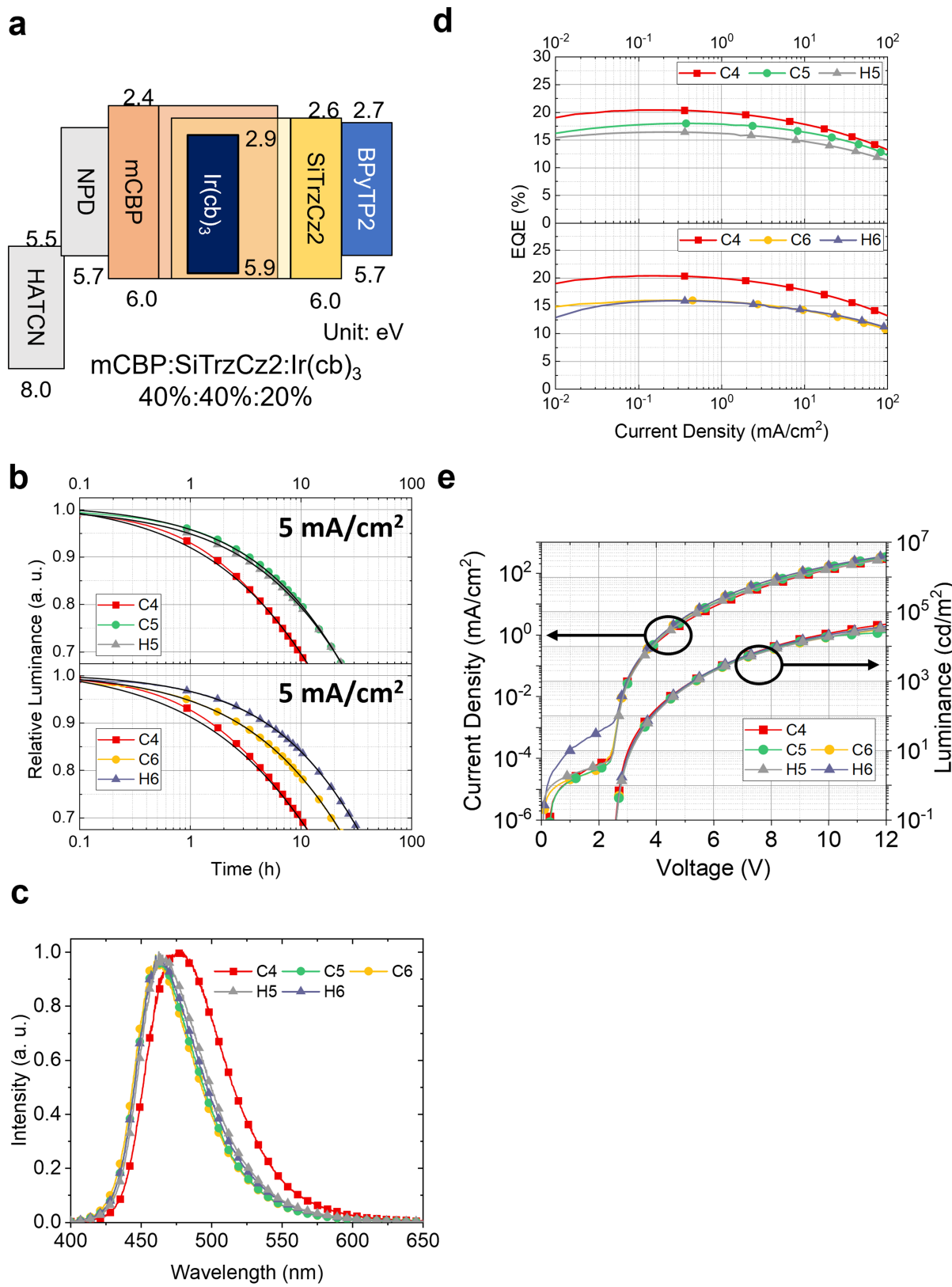
respectively. The PF for isotropic dipoles is averaged over 67% horizontal (in-plane) and 33% vertical (orange line) dipoles. The measured PF of horizontal dipoles is labelled by diamonds at 45 nm from the cathode, corresponding to the centre of the 50-nm-thick EML. The simulated centre wavelength is 465 nm. **c**, Simulated PF of isotropic dipoles in half cavities H versus wavelength overlapped with the Ir(dmp)₃ PL spectrum. The exciton is located at 36 nm from the interfaces of Ag/BPYTP2, Al/BPYTP2, Ag/SF3Trz and Al/SF3Trz. **d**, Measured normalized decay rate, $k_r/k_{r,0}$ overlaid with the simulated PFs for horizontal (PF_{hor}) and isotropic (PF_{iso}) dipoles using the Green's function method^{31,32}. Here $k_{r,0}$ is the decay rate of the bare EML.



Extended Data Fig. 5 | Ir(dmp)₃ device energy levels and performance.

a, Device structure and frontier orbital levels (in eV). **b**, EQE versus J of C1–C3, H1–H3 and F1–F3. EQE data are averaged from at least from two different batches with two devices in each batch. **c**, EL spectra of C1–C3, H1–H3 and F1–F3 at $J = 10 \text{ mA cm}^{-2}$. Inset, chromaticity coordinates of the devices. The arrow indicates the blueshift from the control to the full-cavity devices. **d**, Current–voltage (J – V , left axis) and luminance (right axis) characteristics of C1–C3, H1–H3

and F1–F3. **e**, Device operational lifetime for C1–C3, H1–H3 and F1–F3 at $J = 7 \text{ mA cm}^{-2}$. For C1–C3, H1–H3 and F1, lifetime data are shown from two devices in different batches. For F2 and F3, lifetime data are shown from three devices in different batches. Shaded area indicates the 95% confidence interval. Solid black lines are fits to a stretched exponential: $L(t)/L_0 = \exp[-(t/t_0)^\beta]$ for C and F devices, in which L_0 is the initial luminance and t_0 and β are parameters (see Extended Data Table 2).



Extended Data Fig. 6 | Ir(cb)₃ device energy levels and performance. **a**, Device structure and frontier orbital levels (in eV). **b**, Device operational lifetime at $J = 5 \text{ mA cm}^{-2}$. Errors are indicated in Extended Data Table 1. Average from three devices for each curve. Solid black lines are fits to a stretched exponential: $L(t)/L_0 = \exp[-(t/t_0)^\beta]$, in which L_0 is the initial luminance and t_0 and β are

parameters (see Extended Data Table 2). **c**, EL spectra of C4–C6 and H5 and H6 at $J = 10 \text{ mA cm}^{-2}$. **d**, EQE versus J of C4, C5 and C6 and H5 and H6. Errors are indicated in Extended Data Table 1. Average from three devices for each curve. **e**, J – V (left axis) and luminance (right axis) characteristics of C4–C6 and H5 and H6.

Extended Data Table 1 | Summary of Ir(dmp)₃ and Ir(cb)₃ device performance

No.	Phosphor	Optical structure ^a	EQE _{max} (%) ^b	Calc. PF _{avg} ^c	CIE	L ₀ (cd/m ²)	LT90 (h) ^d	LT80 (h) ^d	LT70 (h) ^d
at 7 mA/cm ²									
C1	Ir(dmp) ₃	Al/SF3Trz 17nm/... /ITO	7.2 ± 0.1	1.4 ± 0.1	(0.16, 0.26)	770 ± 10	30 ± 5	100 ± 10	200 ± 30
H1		Ag/SF3Trz 17nm/... /ITO	6.5 ± 0.1	2.0 ± 0.2	(0.16, 0.26)	750 ± 10	80 ± 4	213 ± 8	390 ± 20
F1		Ag/SF3Trz 17nm/... /DBR	7.4 ± 0.2	1.9 ± 0.2	(0.14, 0.14)	500 ± 20	75 ± 10	220 ± 10	400 ± 20
C2		Al/BPyTP2 17nm/... /ITO	7.6 ± 0.1	1.5 ± 0.1	(0.16, 0.25)	880 ± 10	36 ± 2	140 ± 10	280 ± 20
H2		Ag/BPyTP2 17nm/... /ITO	6.5 ± 0.1	2.4 ± 0.2	(0.17, 0.28)	800 ± 10	100 ± 10	340 ± 30	630 ± 60
F2		Ag/BPyTP2 17nm/... /DBR	6.3 ± 0.3	2.4 ± 0.2	(0.14, 0.18)	530 ± 20	160 ± 30	390 ± 50	700 ± 50
C3		Al/BPyTP2 25nm/... /ITO	9.9 ± 0.1	1.4 ± 0.1	(0.16, 0.27)	1030 ± 10	50 ± 3	172 ± 7	370 ± 15
H3		Ag/BPyTP2 25nm/... /ITO	9.0 ± 0.1	2.0 ± 0.2	(0.17, 0.32)	1000 ± 10	80 ± 3	251 ± 4	470 ± 20
F3		Ag/BPyTP2 25nm/... /DBR	10.4 ± 0.5	2.0 ± 0.2	(0.15, 0.20)	800 ± 50	110 ± 20	280 ± 20	430 ± 20
at 5 mA/cm ²									
C4	Ir(cb) ₃	Al/BPyTP2 40nm/... /ITO	20.4 ± 0.5	1.4 ± 0.1	(0.14, 0.26)	1350 ± 20	1.6 ± 0.1	4.6 ± 0.1	9.6 ± 0.1
C5		Al/BPyTP2 20nm/... /ITO	18.0 ± 0.2	1.5 ± 0.1	(0.14, 0.15)	1050 ± 20	3.4 ± 0.1	9.9 ± 0.1	20.1 ± 0.1
H5		Ag/BPyTP2 20nm/... /ITO	16.4 ± 0.2	2.1 ± 0.2	(0.14, 0.17)	1020 ± 20	2.9 ± 0.1	9.6 ± 0.2	20.0 ± 0.3
C6		Al/BPyTP2 15nm/... /ITO	16.0 ± 0.1	1.6 ± 0.1	(0.14, 0.14)	910 ± 20	2.7 ± 0.1	9.0 ± 0.1	18.7 ± 0.1
H6		Ag/BPyTP2 15nm/... /ITO	15.9 ± 0.2	2.4 ± 0.2	(0.14, 0.16)	930 ± 20	5.3 ± 0.1	14.9 ± 0.1	29.3 ± 0.1

^a See Extended Data Fig. 3 for details.

^bThe natural photoluminescence quantum yield of the bare EML is $\eta_{PL,0} = 85 \pm 8\%$ ¹⁶ for Ir(cb)₃ and $\eta_{PL,0} = 44 \pm 1\%$ ¹¹ for Ir(dmp)₃.

^cThe average Purcell factors PF_{avg} is calculated by averaging across a triplet ensemble with isotropic dipole orientation: $PF_{avg} = 2/3 PF_{horiz.} + 1/3 PF_{vert.}$. Here, PF s of horizontal and vertical dipoles are $PF_{horiz.}$ and $PF_{vert.}$, respectively.

^dDevice lifetime data at constant current density are extracted from Extended Data Figs. 5e and 6b.

Measured EQE, CIE, initial luminance L₀, LT90, LT80 and LT70 and the calculated average PF for Ir(dmp)₃ devices C1–C3, H1–H3 and F1–F3 and Ir(cb)₃ devices C4–C6 and H5 and H6. Ir(dmp)₃ devices are aged at the same current density J=7mAcm⁻². Ir(cb)₃ devices are aged at the same current density J=5mAcm⁻².

Article

Extended Data Table 2 | Summary of stretched exponential model for $\text{Ir}(\text{dmp})_3$ and $\text{Ir}(\text{cb})_3$ devices

No.	Phosphor	Stretched Exp. Model	
		t_0 (h)	β
C1	$\text{Ir}(\text{dmp})_3$	900 \pm 40	0.67 \pm 0.01
H1		1600 \pm 40	0.77 \pm 0.01
F1		1650 \pm 60	0.65 \pm 0.01
C2		1290 \pm 20	0.65 \pm 0.01
H2		3600 \pm 150	0.63 \pm 0.01
F2		2680 \pm 80	0.78 \pm 0.01
C3		1730 \pm 90	0.64 \pm 0.01
H3		2150 \pm 80	0.69 \pm 0.01
F3		2200 \pm 120	0.72 \pm 0.01
		t_0 (h)	β
C4	$\text{Ir}(\text{cb})_3$	55.0 \pm 0.1	0.57 \pm 0.01
C5		95.7 \pm 0.1	0.64 \pm 0.01
H5		104.0 \pm 0.1	0.62 \pm 0.01
C6		102.5 \pm 0.1	0.60 \pm 0.01
H6		131.0 \pm 0.1	0.67 \pm 0.01

Stretched exponential model: $L(t)/L_0 = \exp[-(t/t_0)^\beta]$. Fit parameters t_0 and β are shown for C1–C3, H1–H3 and F1–F3 lifetime data in Extended Data Fig. 5e and C4–C6 and H5 and H6 lifetime data in Extended Data Fig. 6b.